

B.A.T. Noordman<sup>1</sup>, W.J. Vankan<sup>2</sup>

<sup>1</sup>Royal Netherlands Aerospace Centre, Marknesse, The Netherlands <sup>2</sup>Royal Netherlands Aerospace Centre, Amsterdam, The Netherlands

E-mail: Bram.Noordman@nlr.nl

#### **Abstract**

Future aircraft have to comply with strict environmental targets like reductions in CO<sub>2</sub>, NO<sub>x</sub> and noise emissions. Ultra-High Bypass Ratio (UHBR) turbofan engines with large fan diameters are promising in terms of reduction of fuel consumption and emissions. To investigate the challenging integration of such an UHBR engine in the airframe, an experimental scaled turbofan model is being developed to perform a wind tunnel test campaign. For the fan stage of this turbofan model composite fan blades are designed that shall resist the high centrifugal and aerodynamic loads for different flight conditions. For the design and analyses of the composite fan blade, a detailed finite element method (FEM) modelling approach is developed taking into account accurately the 3D blade geometry including blade foot, composite material properties, fibre directions and composite layup of the blade design. This detailed FEM modelling approach is validated with test results of geometrically simplified composite test elements. Blade hot-to-cold analyses are applied to the Aerodynamic Design Point (ADP-S1) flight condition to retrieve the blades' cold shape that will be manufactured. With the cold shape of the blade design the hot shapes are calculated for different flight conditions and blade twist angles and blade tip radial displacements are checked. Campbell diagrams for the blade design are generated for the first 3 eigenmodes to assess the blade's vibrational behaviour under operational conditions. The first three blade eigenfrequencies at zero rotational speed were compared with test blade tap test results, which agreed guite well.

**Keywords:** turbofan engine, finite element method, carbon reinforced composite material, aero-acoustics, Campbell diagram

#### 1. Introduction

In the context of the Clean Sky 2 JU Horizon 2020 project 'Support to future CROR and UHBR Propulsion system Maturation (PropMat)' [1] a composite UHBR fan blade was designed and analysed as part of an experimental UHBR turbofan engine in close operation with industrial partner Airbus. For the design and analysis of this composite fan blade a detailed finite element approach was developed, which can take into account accurately the blade geometry including blade foot, composite material properties, fibre directions and composite layup.

# 1.1 UHBR turbofan engine test rig

The aero-acoustic behaviour of UHBR turbofan engine will be tested in wind tunnel test campaigns as part of the Clean Sky 2 project 'Simulator of Aerodynamic and Acoustic Fan IntegRation (SA²FIR)' ([2], [3]) in cooperation with Airbus. The SA²FIR test rig, see Figure 1, will contain a highly detailed scaled instance of a representative UHBR turbofan engine that will be tested in various low-speed and high-speed wind tunnel conditions at DNW Large Low-speed Facility (LLF) [4] in the Netherlands and in the ONERA S1MA [5] wind tunnel in France. The fan rotor, which is important for the engine's aero-acoustic behaviour, contains very specifically designed and instrumented carbon composite fan blades, which will have to resist high centrifugal and aero loads.

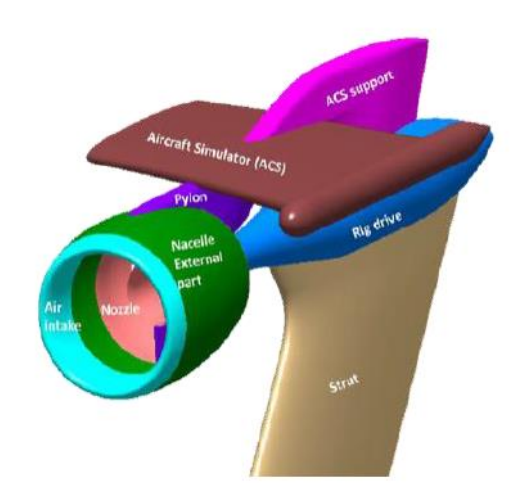


Figure 1 - SA<sup>2</sup>FIR test rig.

The final resulting fan blade geometry, the so-called 'design shape', represents the fan blade in its nominal operating condition (or operating point, OP). This nominal operating condition is based on the so-called 'Aerodynamic Design Point' (ADP), that corresponds to the cruise condition of the full-scale aircraft. The Fan and Compressor Department of the German Aerospace Center (DLR) has iteratively improved the fan blade design shape with Computational Fluid Dynamics (CFD) analyses and handed the final optimal blade design shape over to NLR for the structural analyses. The initial rotor blade design is based on a full-scale engine realistic fan design by DLR as part of a propulsion system with intake and exhaust system designed by Airbus [6].

# 1.2 Detailed finite element approach for fan blade design and analysis

To achieve the required accurate representation of the fan blade geometry, carbon composite orientations and properties, a detailed finite element (FEM) modelling approach has been developed in MATLAB [7] and SIMULIA/Abaqus [8] for FEM analysis and postprocessing. This approach is flexible and efficient and uses as inputs only the aerodynamic surface representation of the blade in design shape, the blade foot geometry and the composite ply properties and composite layup definition. Loads are derived from the aerodynamic and centrifugal forces in the different operational conditions. In the FEM modelling approach for the composite blade, the 3D locations of the leading edge (LE), trailing edge (TE) and mid surface are derived from the 3D coordinates of the blade geometry. With the LE and TE locations and the air foil lines the camber lines are derived at each of the span wise stations. From these camber lines the mid surface is composed, see the green surface at the blade root in Figure 2. The blade geometry is meshed both with linear hexahedral elements (type C3D8 in Abaqus, see Figure 3) as well as with linear shell elements (type S4, on mid surface of blade). The local blade thickness is determined by the distance, perpendicular to the mid surface, between pressure and suction sides.

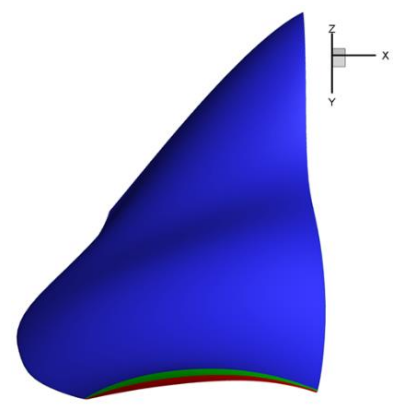


Figure 2 - Example of the 3D blade design shape (suction side (blue), mid (green) and pressure side (red) surfaces).

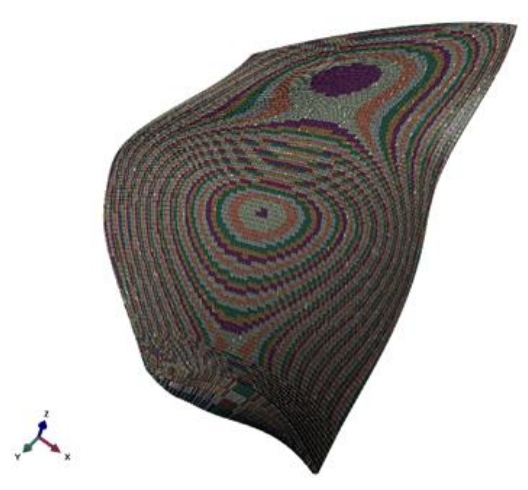


Figure 3 - Solid FEM mesh of final blade design shape with approximate/extended foot geometry.

The composite blades are manufactured at NLR with the closed mould press process from unidirectional (UD) plies. The plies will be stacked in the mould from suction side to pressure side (or vice versa), with a symmetric layup and ply drops in the mid surface. The thickness and layup of the blade vary strongly between LE and TE and blade foot and blade tip.

# 2. Test element modelling and results

The composite ply properties are largely based on the known design allowables of a carbon fibre reinforced thermoset composite material from literature and some extra coupon tests performed at NLR. These values were translated to ply properties assuming an aimed Fibre Volume Fraction (FVF) of 58% and a void content of 0% for the press process.

#### 2.1 Finite element model of test element

To validate the detailed blade FEM modelling approach, some test elements were manufactured at NLR, amongst others so-called 2.5D test elements with a single and double foot and 3D test elements with a twist angle both for the single and as well as for double foot versions (see Figure 4 and Figure 5). With these test elements static and eigenfrequency tests were performed. The test elements were assigned a composite layup similar to the blade's layup. In the thinner centre sections of the test elements the ply drops occur in the mid surface, i.e. the 0 degree plies are dropped with the length direction of the test elements as the reference direction for the layup, i.e. the zero degree fibre angle orientation.

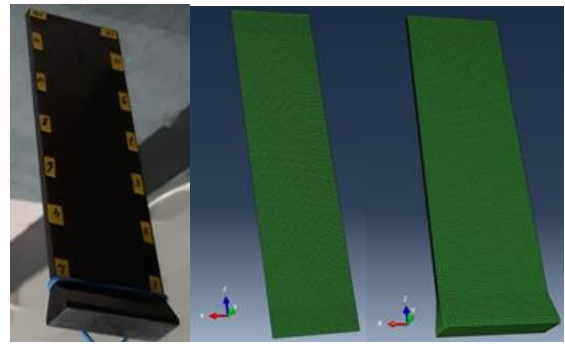


Figure 4 - Physical 2.5D test element with single foot (left) with shell (middle) and solid (right) FEM models of 2.5D test element.

The material properties of the carbon fibre reinforced thermoset composite material were used for the test element FEM models, but the fibre dominated Young's modulus E11 (average of tension and compression values) and the ply density were corrected for the actual measured FVF of the test element. All matrix dominated properties were used without any modification.

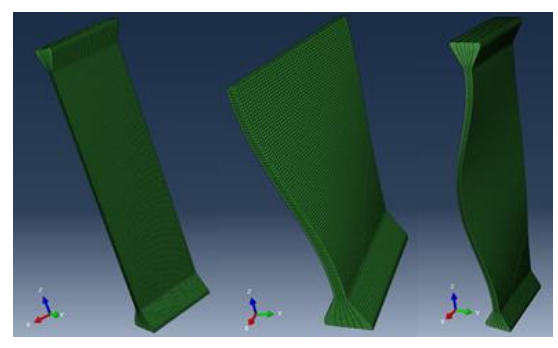


Figure 5 - Solid FEM models of 2.5D test element with double foot (left), 3D test element with single foot (middle) and 3D test element with double foot (right).

# 2.2 Test element results

The eigenfrequency results of the shell and solid FEM model of a test element with single foot and free-free boundary condition and the eigenfrequencies found by acoustic measurement with specimen label 7822 are given in Table 1. All eigenfrequencies of the test are predicted within 3.5% error margins by the shell and solid model. The solid model is more accurate in predicting the bending eigenfrequencies and the shell model is more accurate in predicting the torsion frequencies. The mode shapes of the solid model with free-free boundary conditions are shown in Figure 6.

Table 1 - Eigenfrequencies from the acoustic tests and the solid and shell FEM model of test element 7822 with single foot and free-free boundary condition.

Specimen label	Mass [gr]	Mode 1 1 <sup>st</sup> bending I <sub>xx</sub> [Hz]	Mode 2 1 <sup>st</sup> torsion [Hz]	Mode 3 $2^{nd}$ bending $I_{xx}$ [Hz]
7822 (acoustic test)	67.7	822.0	1811.0	2378.0
Shell model	67.8	824.8	1844.8	2394.0
Difference with test [%]	0.2	0.3	1.9	0.7
Solid model	67.7	823.8	1874.2	2386.5
Difference with test [%]	0.0	0.2	3.5	0.4

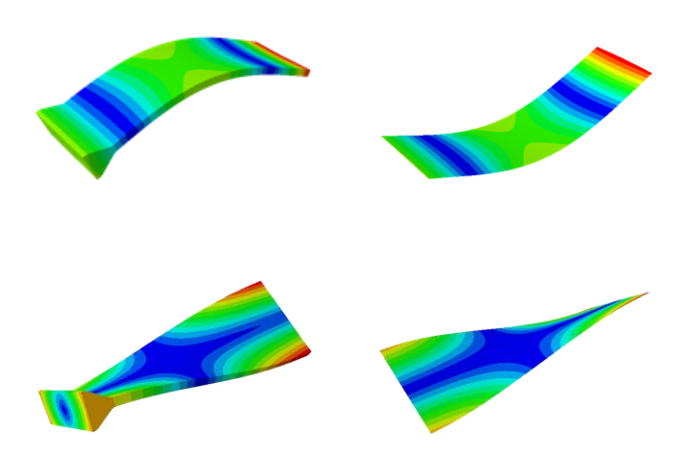


Figure 6 - Bending (top) and torsion (bottom) mode shapes of solid (left) and shell (right) FEM model of test element 7822 with single foot and free-free boundary condition.

The 2.5D element 7822 with single foot was also modelled with fixed-free boundary conditions and compared to experimental results. For the fixed boundary condition the area at the inclined surfaces of the foot was restrained in the shell and solid model. All other model parameters were left unchanged compared to the free-free boundary condition. The results are shown in Table 2. The largest difference with the test found here is 6.1% for the shell model at the second bending eigenfrequency.

Table 2 - Eigenfrequencies from the acoustic tests and the solid and shell FEM model of test element 7822 with single foot and fixed-free boundary condition.

Specimen label	Mass [gr]	Mode 1 1 <sup>st</sup> bending I <sub>xx</sub> [Hz]	Mode 2 2 <sup>nd</sup> bending I <sub>xx</sub> [Hz]	Mode 3 1 <sup>st</sup> torsion [Hz]
7822 (acoustic test)	67.7	188.0	1087.0	1173.0
Shell model	67.8	188.9	1153.2	1211.4
Difference with test [%]	0.2	0.5	6.1	3.3
Solid model	67.7	185.5	1136.9	1229.2
Difference with test [%]	0.0	-1.4	4.6	4.8

Also a 3-point bending test was performed according to test standard ASTM D7264 with 2.5D test element 7822, see Figure 7, for further validation of the static bending stiffness of the solid and shell FEM models. The experimental test was performed with a support span length of  $L=120\,\mathrm{mm}$  on cylindrical supports with a diameter of 10 mm. In the experiment a 2 kN force was applied to the test element at half the span length with a 10 mm diameter cylindrical loading indenter at a test speed of 0.5 mm/min at room temperature.



Figure 7 - Experimental 3-point bending test setup of test element 7822 with single foot.

The 3-point bending test with 2.5D test element 7822 was also simulated with the solid and shell model. The boundary condition of the left support in the experiment was modelled by restraining the translation in global y- and z-direction, see Figure 8. The right support was modelled by restraining the translation in global z-direction. Additionally the displacement in the global x-direction was suppressed at one point of the left support. The indenter was modelled as a discrete rigid with a rigid body constraint. A 2 kN load was applied to the reference point of the indenter in a geometric nonlinear static analysis step after a static step to initiate the contact between indenter and test element. A surface-to-surface finite sliding contact was defined with a hard contact definition for normal contact and a friction coefficient of 0.25 was used for tangential behaviour.



Figure 8 - Solid FEM model of 3-point bending test of 2.5D test element 7822 with single foot.

The applied force P at the outer surface at mid-span of the real test element in the experiment and of the shell and solid models are shown in Figure 9 versus the mid-span deflection  $\delta$ .

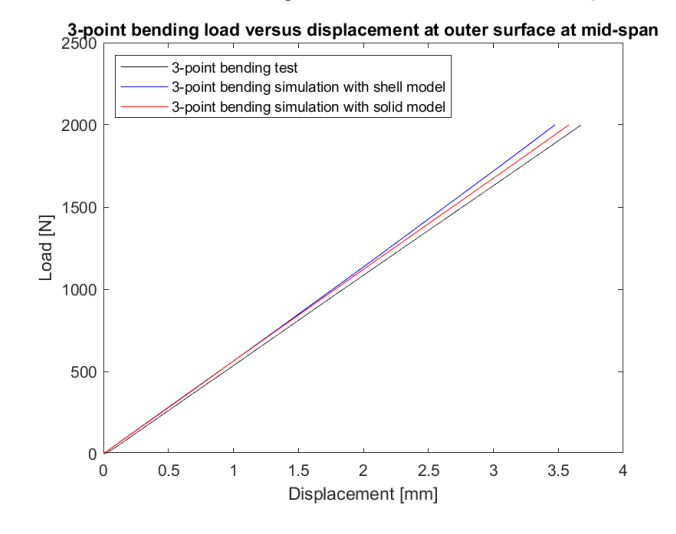


Figure 9 - Three-point bending force versus mid-span deflection of 2.5D test element 7822 with single foot.

The solid test element FEM model behaves less stiff than the shell FEM model, which agrees with the predicted bending eigenfrequencies, which are lower for the solid model than for the shell model both for free-free and fixed-free boundary condition. The bending stiffness of the shell and solid model are both a bit larger than found with the experiment.

## 3. Fan blade modelling and results

The design shape blade geometry is represented in a FEM model, see e.g. Figure 3, and is considered as the hot shape geometry in a certain load case, here ADP-S1 condition. Therefore the design shape is assumed to be the deformed shape of the blade subjected to ADP-S1 loads.

## 3.1 Blade hot-to-cold analysis results

The blade's un-deformed shape is calculated by FEM simulation in an iterative procedure both for the shell and solid blade FEM model with approximated foot, here referred to as the blade's hot-to-cold transformation. The blade cold shape is determined in an iterative inverse static deformation calculation. This cold shape is specific for the considered design shape, for the blade's properties like composite material and layup, and for the design shape load case conditions like rotation speed, aerodynamic loads and boundary conditions. The final cold shape of the composite blade that resulted from the hot-to-cold analysis (H2C) analysis with the shell model is shown in Figure 10. It should be noted that the DLR design shape does not contain the definition of the blade foot, but the FEM models do contain an approximated foot. Both the shell FEM and the solid FEM H2C analyses gave consistent results for the cold shape. The H2C analyses converged in 10 iterations to residuals of the nodal coordinates that are below 2e-7 mm. This means that for the ADP-S1 hot shape the nodal coordinates are all less than 2e-7 mm away from their corresponding design shape's nodal coordinates.

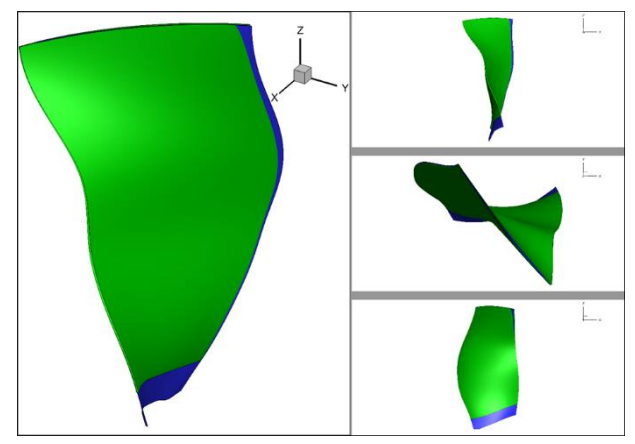


Figure 10 - Comparison between the DLR blade design shape (in green) and the shell FEM blade cold shape (in blue).

# 3.2 Blade cold-to-hot analysis results

The shell and solid FEM model of the blade cold shape with extended foot were used to analyse blade deformations for all the operating points (OPs) with restrained blade foot that is placed in a hub. We find good correspondence between the deformations of the shell and solid FEM models. For instance, we find very similar deformation patterns for the ADP-S1 OP in both FEM models. The maximum displacement in both models is in the trailing edge tip corner of the blade (see Figure 11), and has values of 1.331 mm and 1.366 mm for the shell and solid FEM models, respectively, i.e. a difference of about 2.6%.

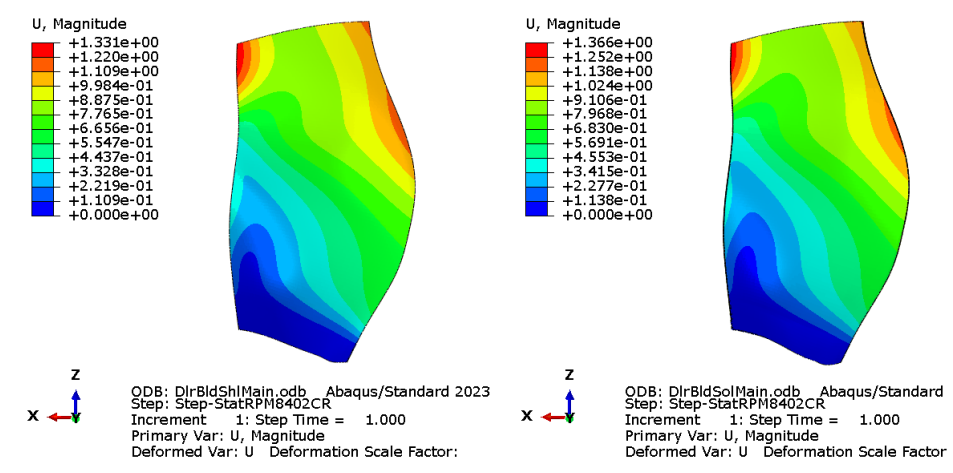


Figure 11 - Blade deformation results for shell and solid FEM models of DLR design for ADP-S1 load case.

From the blade cold-to-hot (C2H) analysis results the blade twist change and the blade tip extension were also determined for all OPs. The blade twist is defined as the angle between chord-lines at different span locations, see Figure 12.

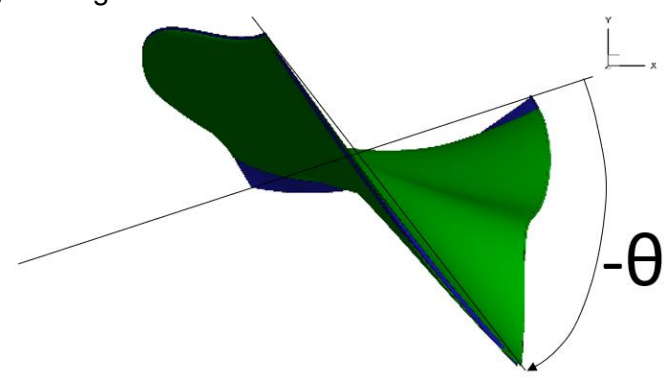


Figure 12 - Blade twist angle definition.

The blade twist angle as function of the TE span wise location is shown in Figure 13 for all the OPs. It can be seen from the top figure that the total twist angle becomes less negative with respect to the cold shape for all OPs. The hot-to-hot (H2H) twist angles of the blade as shown in the bottom figure are defined as the twist angle in the OP minus the twist angle for load case ADP-S1.

The blade tip radius of the blade shell model as a function of the chordwise location is shown in Figure 14. The largest blade tip radius occurs at the trailing edge in load case MFC-S1, which has the largest centrifugal load. It must be noted the blade FEM model is based on CFD geometry, which includes the 0.2 mm tip gap. So the actual blade tip radius for all curves is 0.2 mm lower. But Figure 14 does illustrate well which load case has the smallest tip gap between the blade tip and the nacelle shroud.

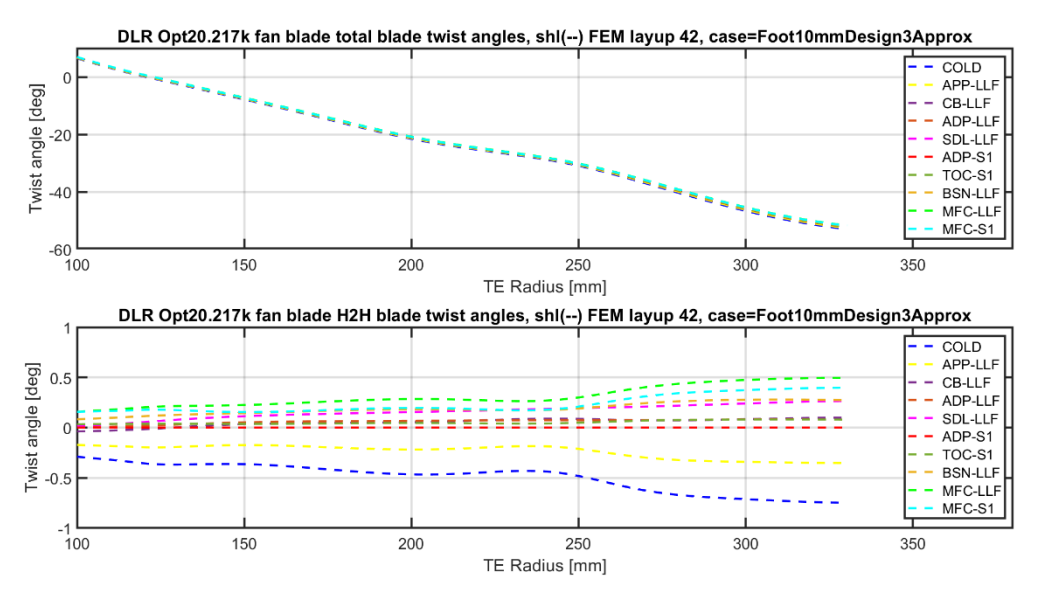


Figure 13 - Total twist angle (top) and hot-to-hot twist angle (bottom) found with shell blade model for all OPs.

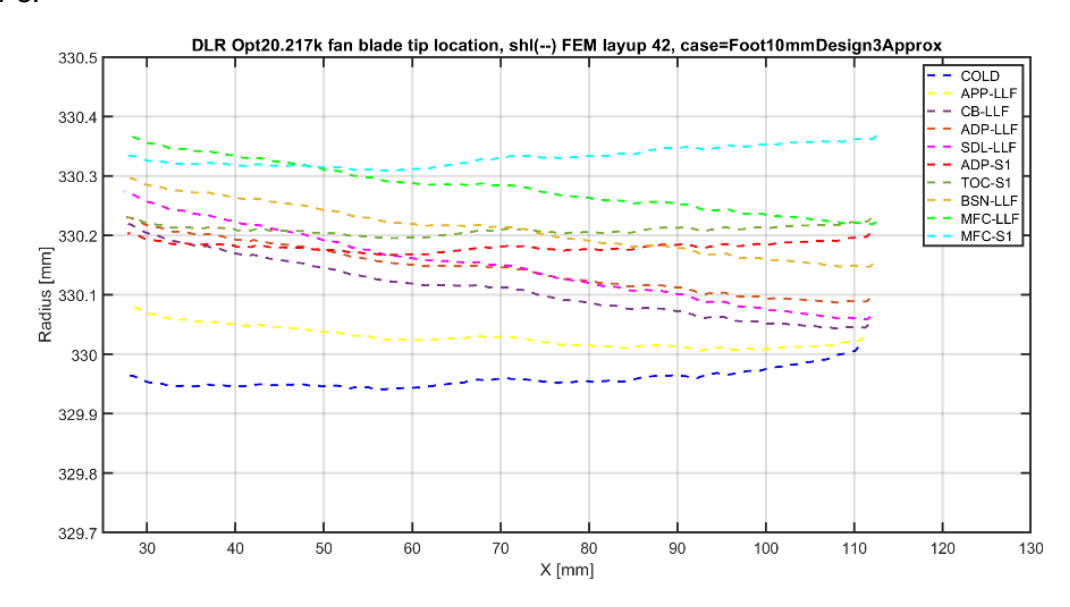


Figure 14 - The blade tip radius as function of the chordwise location for shell blade model for all the OPs.

The Campbell diagram to assess the vibration behaviour of the blade is shown in Figure 15 for both the shell and solid model of the blade FEM model with extended foot. The foot was clamped over a length of approximately 10 mm in span direction. The bottom 2 curves are the bending eigenfrequencies of the shell and solid blade model increasing with rotation speed and the top curve is of the first torsion eigenfrequency of the blade, which is flatter. Sufficient separation between first

torsion mode and second bending mode was assured and crossings of modes 1-3 with lower engine orders were avoided. Frequency increases due to aeroelastic effects were not investigated and are assumed small.

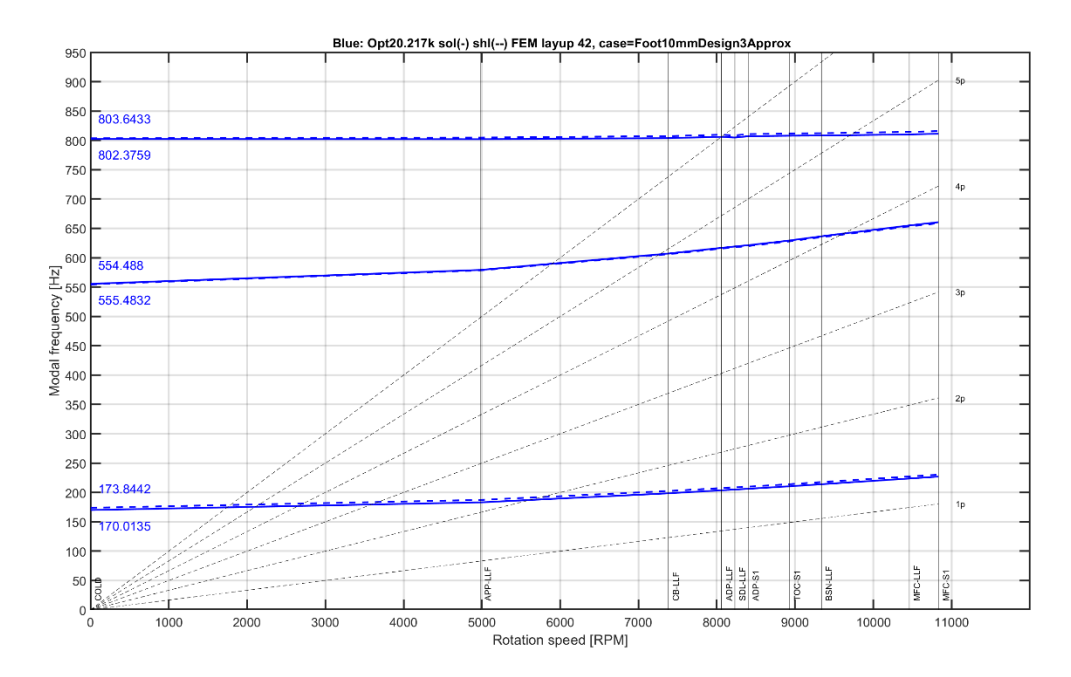


Figure 15 - Campbell diagram for shell and solid blade FEM model.

## 3.3 Fan blade results with detailed foot model

During the PropMat project the blade foot design had to be updated to create more space at the trailing edge for parts behind the fan rotor. Therefore material was cut from the blade foot trailing edge. To assess the influence of this reduced blade foot width on the Campbell diagram and for an accurate blade foot stress assessment in the SA2FIR project, a more detailed blade foot model was developed which was coupled to the blade shell model with a shell-to-solid coupling constraint. The blade foot geometry had to be slightly adapted (small extensions at LE and TE of foot) in order to define a proper block-structured solid mesh in the foot, see Figure 16. This block-structured solid mesh is needed for implementing the composite layup definition, for which the same layup definition has been used as for the blade.

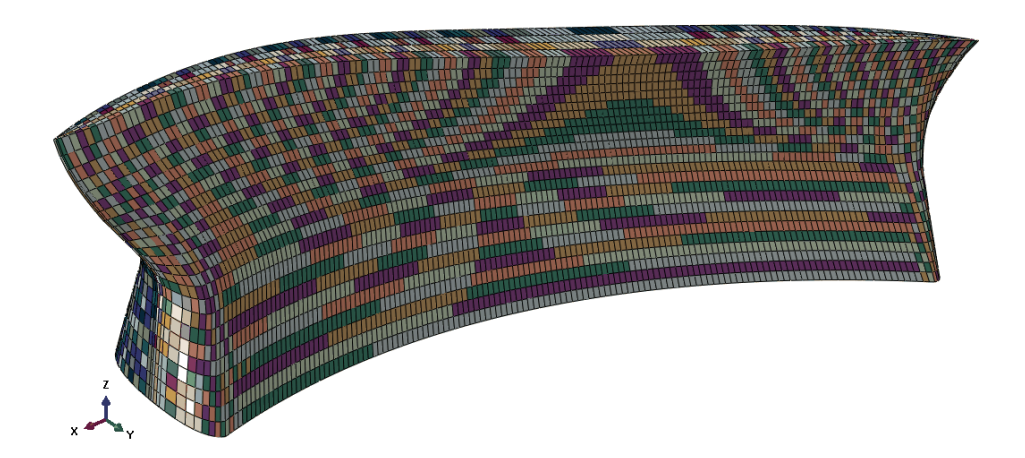


Figure 16 - Detailed solid FEM foot model.

The Campbell diagram of the shell blade model coupled to the detailed solid foot model is shown in Figure 17. Very similar values for the eigenfrequencies are found as for the previous model, except for the second bending mode where the frequency is a bit higher, i.e. 563.3 Hz versus 555.5 Hz at 0 RPM, so about 1.4 % difference. The eigenfrequencies at 0 RPM agree quite well with preliminary average tap test results of 3 manufactured test blades, which gives 170.58 Hz for the first bending

eigenfrequency and 562.24 Hz for second bending eigenfrequency. The measured first torsion eigenfrequency was 762.51 Hz, which is still a bit overpredicted by the shell blade model with detailed foot.

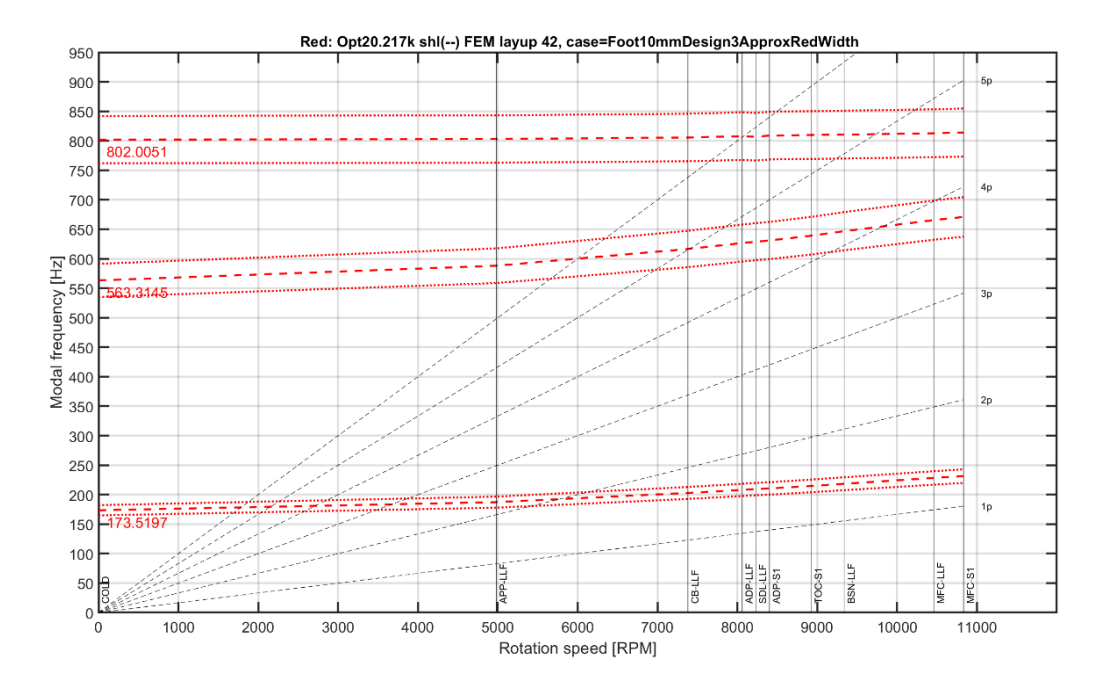


Figure 17 - Campbell diagram found for shell blade model coupled to solid detailed foot model.

Instead of fixing the detailed blade foot, also a foot contact analysis was performed with a discrete rigid hub surface surrounding the foot, see Figure 18. In the foot contact analysis a surface-to-surface contact was used with hard contact definition for normal behaviour and friction coefficient  $\mu$  = 0.3 was used for tangential behaviour, because in the manufactured blades metal strips will be added to the contact surfaces of the composite foot.

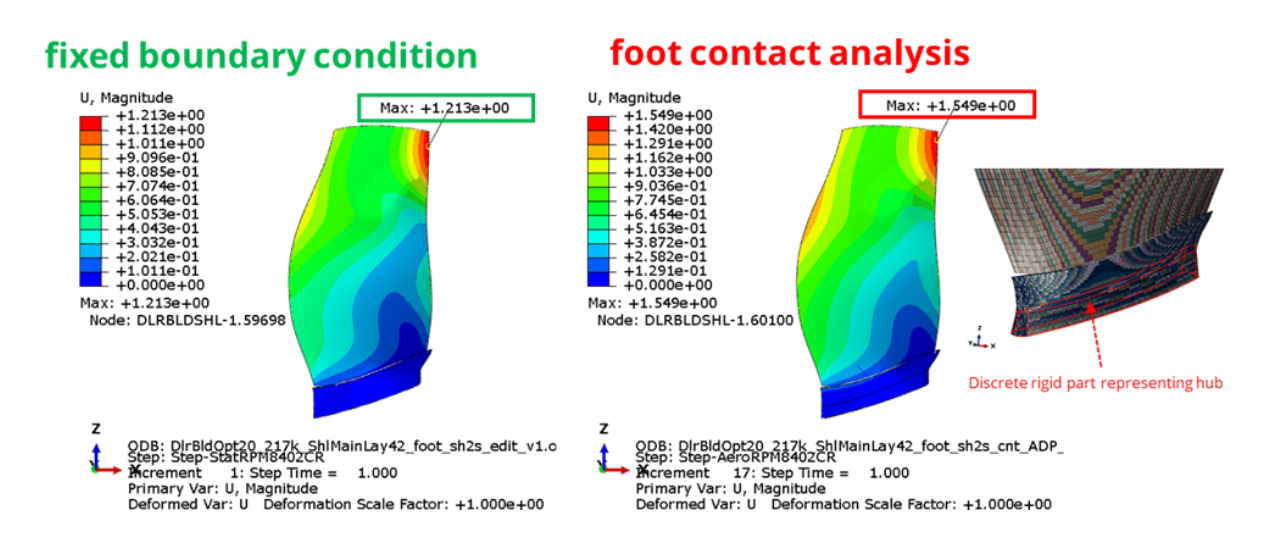


Figure 18 - Blade deformation result for shell model of DLR design with detailed foot for ADP-S1 load case with fixed boundary condition (left) and contact analysis (right).

In the foot contact analysis a slightly larger blade displacement than in the analysis with fixed boundary condition was found, up to about 0.34 mm larger, especially in the blade tip trailing edge area, which means that the resulting hot shape will deviate from the design shape. To compensate for these undesirable deviations that are due to the slip between foot and hub, small rigid prerotations were applied to the blade and foot relative to the hub, which was carried out for the SA2FIR project and is not part of this paper.

#### 4. Conclusions

A detailed finite element approach was successfully developed for the design and analysis of an UHBR composite fan blade, which can take into account accurately the blade geometry including blade foot, composite material properties, fibre directions and composite layup. The method was validated with test results of composite test elements and test blades showing a difference between simulation and experimental results of only a few percent. The blade modelling method can also be used for other types of composite structures like propeller blades.

### Contact Author Email Address

mailto: Bram.Noordman@nlr.nl

# **Copyright Statement**

The authors confirm that they, and/or their company or organization, hold copyright on all of the original material included in this paper. The authors also confirm that they have obtained permission, from the copyright holder of any third party material included in this paper, to publish it as part of their paper. The authors confirm that they give permission, or have obtained permission from the copyright holder of this paper, for the publication and distribution of this paper as part of the ICAS proceedings or as individual off-prints from the proceedings.

# **Acknowledgements**

The PropMat project has received funding from the Clean Sky 2 Joint Undertaking under the European Union's Horizon 2020 research and innovation programme under grant agreement No 680954.

#### **Disclaimer**

The document reflects only the author's view; the JU is not responsible for any use made of the information contained herein. This work has been performed in close cooperation with Airbus and DLR.





## References

- [1] PropMat project. https://cordis.europa.eu/project/id/680954.
- [2] SA<sup>2</sup>FIR project. <a href="https://www.clean-aviation.eu/media/results-stories/integration-of-advanced-propulsion-engines-makes-headway">https://www.clean-aviation.eu/media/results-stories/integration-of-advanced-propulsion-engines-makes-headway</a>.
- [3] Faasse PR, Baardman R and Van Zutphen WJCM. Real-time acquisition, processing and visualization of large datasets during a wind tunnel campaign. *European Test & Telemetry Conference (ETTC)*, Toulouse, France, 2023.
- [4] DNW LLF wind tunnel. https://www.dnw.aero/wind-tunnels/llf/.
- [5] ONERA S1MA wind Tunnel. <a href="https://www.onera.fr/en/windtunnel/s1ma-continuous-flow-wind-tunnel-atmospheric-mach-005-mach-1">https://www.onera.fr/en/windtunnel/s1ma-continuous-flow-wind-tunnel-atmospheric-mach-005-mach-1</a>.
- [6] Schnell R, Goldhahn E and Julian M. Design and Performance of a Low Fan-Pressure-Ratio Propulsion System. 24th International Symposium on Air Breathing Engines (ISABE), Canberra, Australia, Vol. 1, ISABE-2019-24017, pp 122-137, 2019.
- [7] MATLAB. <a href="https://nl.mathworks.com/products/matlab.html">https://nl.mathworks.com/products/matlab.html</a>.
- [8] SIMULIA. https://www.3ds.com/products/simulia/abagus.